A Branch Current Reallocation Based Energy Balancing Strategy for the Modular Multilevel Matrix Converter Operating Around Equal Frequency

Boran Fan, *Student Member, IEEE*, Kui Wang, *Member, IEEE*, Pat Wheeler, *Senior Member, IEEE*, Chunyang Gu, *Member, IEEE*, and Yongdong Li, *Member, IEEE*

***Abstract*—The modular multilevel matrix converter (M3C) is a promising topology for medium-voltage, high-power applications. Due to the modular structure, it is scalable and capable to produce high quality output waveforms and can be fault tolerant. However, the M3C suffers from low frequency capacitor voltage fluctuation if the output frequency is close to the input voltage frequency, which limits its application in adjustable speed drive fields. This paper presents a theoretical analysis in the phasor domain to find the branch-energy equilibrium point of the M3C when operating with equal input and output frequency first. Then, a branch energy balancing control method based on branch current reallocation is proposed to equalize the energy stored in the nine converter branches. With the proposed method, the M3C can effectively suppress the capacitor voltage fluctuation without injecting common-mode voltage or applying reactive power to the input side. Experimental results are presented to validate the proposed method.**

***Index Terms*—Energy and balancing control, equal frequency, medium-voltage high-power ASD, modular multilevel matrix converter (M3C), triple-star bridge cells (TSBC) converter.**

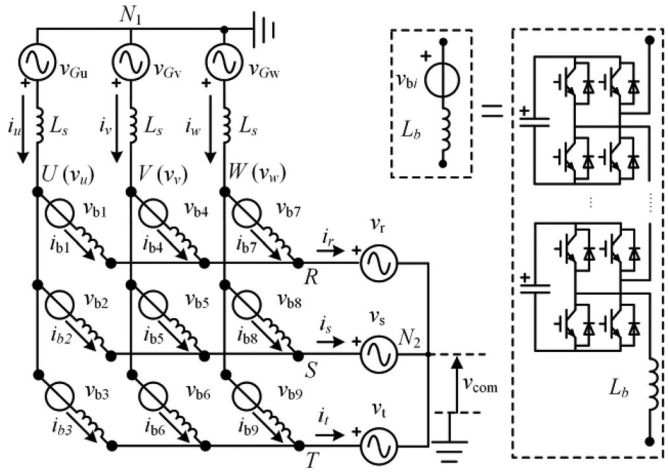

Fig. 1. Circuit configuration of the M3C.

I. Introduction

THE modular multilevel matrix converter (M3C) [1] or triple-star bridge cells converter [2], shown in Fig. 1, can be used to connect two three-phase electrical systems (input side and output side systems) using nine active branches. Each branch is composed of a cascaded connection of full-bridge (H-bridge) converter cells and a branch inductor. The topology enables direct ac–ac bidirectional power conversion and ensures that the three-phase input and output waveforms close to sinusoidal with controllable power factor on the input side [3]–[6]. In common with other members of the modular multilevel cascade converter family [2], the M3C can easily reach high voltage ratings as well as significantly reduce harmonics and electromagnetic interference. In addition, the modular structure makes it easier to accomplish construction, maintenance, and thermal designs. Compared with the back-to-back ac–dc–ac modular multilevel converter (MMC) configuration [7]–[10], recent researches show that the M3C can be more suitable for low-speed constant-torque motor drives [2], [11]–[14].

These advantages make the M3C a promising topology for medium-voltage, high-power adjustable speed drive applications such as off-shore wind-power generations [15], [16], full-electric marine propulsion systems [17], etc. However, the M3C suffers from capacitor voltage fluctuation if the output voltage frequency is close to the input frequency. When the output voltage frequency gets close to the input frequency, the branch power fluctuation can be at a very low frequency (i.e., the difference between input and output frequencies), which will result in significant capacitor voltage fluctuations [18], [19]. This drawback limits the broad frequency range application of the M3C.

In order to solve this problem, [4] presents a solution by injecting circulating currents and applying reactive power at the input side. However, the reactive power at the input side is not permitted in some applications as the input side is connected to the electrical grid. The use of the reactive power may decrease

Manuscript received October 18, 2016; revised January 30, 2017; accepted March 6, 2017. Date of publication March 21, 2017; date of current version November 2, 2017. This work was supported in part by the Education Development Program of Delta Environmental & Educational Foundation under Grant DREK2015001. This paper was presented in part at the 42nd Annual Conference of the IEEE Industrial Electronics Society, Florence, Italy, October 24–27, 2016. Recommended for publication by Associate Editor M. Perez.

B. Fan, K. Wang, and Y. Li are with the State Key Laboratory of Power System, Department of Electrical Engineering, Tsinghua University, Beijing 100084, China (e-mail: fbr13@mails.tsinghua.edu.cn; wangkui@tsinghua.edu.cn; liyd@mail.tsinghua.edu.cn).

P. Wheeler and C. Gu are with the Department of Electrical and Electronic Engineering, University of Nottingham, Nottingham NG7 2RD, U.K. (e-mail: Pat.Wheeler@nottingham.ac.uk; guchunyang@163.com).

Color versions of one or more of the figures in this paper are available online at http://ieeexplore.ieee.org.

Digital Object Identifier 10.1109/TPEL.2017.2685431

grid power quality and increase branch current stresses. The work described in [6] introduces some common-mode voltage to avoid the need for reactive power at the input side, a similar technique to the mitigation control of the MMC at low-speed range [8], [9]. However, the reference for the common mode voltage is difficult to design and may cause over-modulation. The common mode voltage may also lead to premature failure of motor bearings. The ideas described in [20] use an adjustment in the motor voltage to ensure that the input and output side share the same voltage magnitude. This method helps to achieve lower branch current stresses but it has some operational restrictions. The condition of the same input and output voltage magnitude is difficult to hold since in some applications, the voltage levels of the two three-phase systems are different and even if the voltage levels are the same, the condition is still difficult to hold as the motor load changes. In addition, the method in [20] also needs to apply reactive power at the input side.

In order to avoid the use of reactive power and common-mode voltage, this paper discusses an alternative control method that only uses circulating currents in the M3C to equalize the energy among the nine branches. This paper first proves the availability of this consideration and then develops a strategy to design appropriate circulating currents to equalize branch energy. Section II introduces the concept of the "basic branch currents" allocation and explains why the branch energy is unstable under this current allocation. Section III develops an adjusted branch current allocation in phasor domain and reconstructs the branch-energy equilibrium point. Section IV proposes a branch current reallocation method based on the theoretical analysis in Section III. Experimental results are presented in Section V to validate the method, and Section VI concludes the paper.

II. Basic Theory of the M3C

A. Double $\alpha\beta 0$ Transformation

Fig. 1 shows the circuit configuration of the M3C. The M3C connects two three-phase systems using nine branches. In this paper, the input three-phase system are denoted as "UVW" and the output three-phase system are denoted as "RST." In the M3C, each branch consists of a branch inductor L_b and a string of cascaded full-bridges. Applying Kirchhoff's voltage law to nine branches yields

$$[\mathbf{v}_{\boldsymbol{xy\_b}}] = [\mathbf{v}_{Lb}] + [\mathbf{v}_b] = L_b \cdot \frac{d}{dt}[\mathbf{i}_b] + [\mathbf{v}_b] \tag{1}$$

where

$$[\mathbf{v}_{\mathbf{xy\_b}}] = \begin{bmatrix} v_u - v_r & v_u - v_s & v_u - v_t \\ v_v - v_r & v_v - v_s & v_v - v_t \\ v_w - v_r & v_w - v_s & v_w - v_t \end{bmatrix}$$

$$[\mathbf{i}_b] = \begin{bmatrix} i_{b1} & i_{b2} & i_{b3} \\ i_{b4} & i_{b5} & i_{b6} \\ i_{b7} & i_{b8} & i_{b9} \end{bmatrix} \quad [\mathbf{v}_b] = \begin{bmatrix} v_{b1} & v_{b2} & v_{b3} \\ v_{b4} & v_{b5} & v_{b6} \\ v_{b7} & v_{b8} & v_{b9} \end{bmatrix}. \tag{2}$$

$[\mathbf{v}_{\mathbf{xy\_b}}]$ is the matrix of differences between the input and output voltages, $[\mathbf{i}_b]$ is the matrix of branch currents and $[\mathbf{v}_\mathbf{b}]$ is the matrix of output voltages of cascaded full-bridges. The double $\alpha\beta 0$ transformation is used to decouple the current control

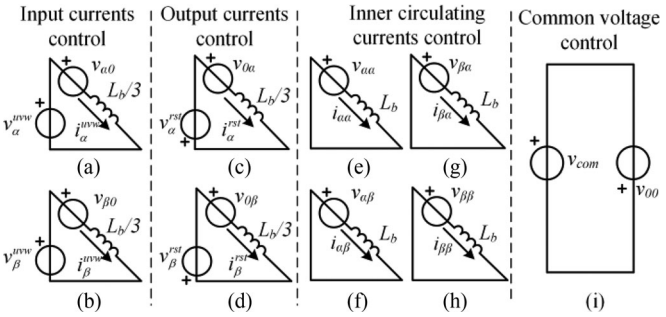

Fig. 2. Equivalent circuits for the M3C.

for the input, output, and internal currents [3]–[6], [20]–[24]. The definition of the double $\alpha\beta 0$ transformation $\boldsymbol{T}_{Dual-\alpha\beta}$ is shown in (3). It is a linear transformation performed on a 3×3 matrix M_{3*3}

$$\mathbf{T}_{Dual-\alpha\beta}(\mathbf{M_{3*3}}) = \mathbf{T}_{\alpha\beta}\mathbf{M_{3*3}}\mathbf{T}_{\alpha\beta}{}^{\mathbf{T}}$$

$$\mathbf{T}_{\alpha\beta} = \frac{1}{3}\begin{bmatrix} 2 & -1 & -1 \\ 0 & \sqrt{3} & -\sqrt{3} \\ 1 & 1 & 1 \end{bmatrix}. \tag{3}$$

Applying this double $\alpha\beta 0$ transformation to (1) yields

$$[\mathbf{v}_{\mathbf{xy\_b}}]_{D-\alpha\beta} = [\mathbf{v}_{Lb}]_{D-\alpha\beta} + [\mathbf{v}_b]_{D-\alpha\beta} = L_\mathrm{b}\frac{d}{dt}[\mathbf{i}_b]_{D-\alpha\beta} + [\mathbf{v}_b]_{D-\alpha\beta} \tag{4}$$

where

$$[\mathbf{i_b}]_{D-\alpha\beta} = \begin{bmatrix} i_{\alpha\alpha} & i_{\alpha\beta} & i_\alpha^{uvw}/3 \\ i_{\beta\alpha} & i_{\beta\beta} & i_\beta^{uvw}/3 \\ i_\alpha^{rst}/3 & i_\beta^{rst}/3 & 0 \end{bmatrix}$$

$$[\mathbf{v_b}]_{D-\alpha\beta} = \begin{bmatrix} v_{\alpha\alpha} & v_{\alpha\beta} & v_{\alpha 0} \\ v_{\beta\alpha} & v_{\beta\beta} & v_{\beta 0} \\ v_{0\alpha} & v_{0\beta} & v_{00} \end{bmatrix}$$

$$[\mathbf{v_{xy\_b}}]_{D-\alpha\beta} = \begin{bmatrix} 0 & 0 & v_\alpha^{uvw} \\ 0 & 0 & v_\beta^{uvw} \\ -v_\alpha^{rst} & -v_\beta^{rst} & -v_{com} \end{bmatrix}. \tag{5}$$

In matrix $[\mathbf{v_{xy\_b}}]_{\mathbf{D-\alpha\beta}}$ and $[\mathbf{i}_b]_{\mathbf{D-\alpha\beta}}$, v_α^{uvw}, v_β^{uvw} and i_α^{uvw}, i_β^{uvw} are the input voltages (v_u, v_v, v_w) and input currents (i_u, i_v, i_w) on the $\alpha\beta$ reference frames. v_α^{rst}, v_β^{rst} and i_α^{rst}, i_β^{rst} are the output voltages (v_r, v_s, v_t) and output currents (i_r, i_s, i_t) on the $\alpha\beta$ reference frames. In matrix $[\mathbf{i}_b]_{\mathbf{D-\alpha\beta}}$, $i_{\alpha\alpha}$, $i_{\alpha\beta}$, $i_{\beta\alpha}$, $i_{\beta\beta}$ are the four inner circulating currents. These four inner circulating currents are independent of input currents (i_u, i_v, i_w) and output currents (i_r, i_s, i_t). They can be used to balance the energy stored in the nine branches. The nine elements in matrix $[\mathbf{v}_b]_{\mathbf{D-\alpha\beta}}$ are the output voltages of the nine cascaded full-bridges on the double $\alpha\beta$ reference frames. Current control for the M3C can be summarized into nine equivalent circuits as shown in Fig. 2 [16]. As shown in Fig. 2, a decoupled control on input, output, and inner

circulating currents can be performed by adjusting the value of matrix $[\mathbf{v}_b]_{\mathbf{D}-\boldsymbol{\alpha\beta}}$.

The value of the common mode voltage v_{com} in Fig. 1 is equal to the value of $' - v'_{00}$ as shown in Fig. 2. In this paper, as the consideration is to avoid the injection of common mode voltage, the value of v_{00} need to satisfy (6). The sum of the nine cascaded full-bridge output voltages is set to be zero.

$$v_{00} = \sum_{i=1}^{9} v_{bi}/9 = -v_{com} = 0. \tag{6}$$

B. Basic Branch Current Allocation

If set the value of circulating currents $i_{\alpha\alpha}$, $i_{\alpha\beta}$, $i_{\beta\alpha}$ and $i_{\beta\beta}$ in $[\mathbf{i}_b]_{\mathbf{D}-\boldsymbol{\alpha\beta}}$ as zero and apply an inverse transformation of $\boldsymbol{T}_{Dual-\alpha\beta}$, the nine branch currents are shown in (7). The branch current consists of 1/3 of the *x*-phase (x = u,v,w) input side current and 1/3 of the *y*-phase (y = r,s,t) output side current

$$\begin{bmatrix} i_{b0,1} & i_{b0,2} & i_{b0,3} \\ i_{b0,4} & i_{b0,5} & i_{b0,6} \\ i_{b0,7} & i_{b0,8} & i_{b0,9} \end{bmatrix} = \frac{1}{3} \cdot \begin{bmatrix} i_u & i_u & i_u \\ i_v & i_v & i_v \\ i_w & i_w & i_w \end{bmatrix} + \frac{1}{3} \cdot \begin{bmatrix} i_r & i_s & i_t \\ i_r & i_s & i_t \\ i_r & i_s & i_t \end{bmatrix}. \tag{7}$$

In this paper, the branch currents in (7) are defined as the "*basic branch currents*." Recent literatures mostly assume this branch current allocation as the "*branch energy equilibrium point*" which implies that this branch current allocation can naturally balance the energy stored among nine branches. On the basis of this allocation, circulating currents $i_{\alpha\alpha}$, $i_{\alpha\beta}$, $i_{\beta\alpha}$ and $i_{\beta\beta}$ are designed to compensate possible branch energy deviations [18]–[20].

C. Branch Power Around Equal Frequency Operation

Here, the input and output systems are assumed to be three-phase balanced. Phase *u/r* is 120° ahead of *v/s* and Phase *v/s* is 120° ahead of *w/t*. AC grid voltages and Input side voltages are defined as

$$v_{Gu} = \hat{v}_{m1}\cos(\omega_1 t) \quad v_u = \hat{v}'_{m1}\cos(\omega_1 t + \gamma_1). \tag{8}$$

In this paper, as the consideration is to apply no reactive power at the ac grid, the input side currents are defined in phase with the ac grid voltages

$$i_u = \hat{i}_{m1}\cos(\omega_1 t). \tag{9}$$

The voltages and currents of the M3C at the output side are defined in (10), where θ is the initial angle difference ($t = 0$) between the output voltage v_r and the input voltage v_u. φ is the power factor angle of the load

$$v_r = \hat{v}_{m2}\cos(\omega_2 t + \theta + \gamma_1) \quad i_r = \hat{i}_{m2}\cos(\omega_2 t + \theta - \varphi + \gamma_1). \tag{10}$$

For simplicity, neglecting the branch inductor L_b and ac inductor L_s ($\gamma_1 \approx 0$, $\hat{v}_{m1} \approx \hat{v}'_{m1}$), the branch power is in (11) when the basic branch current allocation in (7) is applied. It consists of frequency components at ω_1–ω_2, $\omega_1 + \omega_2$, $2\omega_1$ and $2\omega_2$

$$\begin{aligned} p_{bi} &= (v_x - v_y)(i_x + i_y)/3 \\ &= p_{bi}|_{\omega=\omega 1-\omega 2} + p_{bi}|_{\omega=\omega 1+\omega 2} + p_{bi}|_{\omega=2\omega 1} + p_{bi}|_{\omega=2\omega 2}. \\ &(x = u, v, w \;\; y = r, s, t \;\; i = 1, 2, \ldots 9) \end{aligned} \tag{11}$$

Taking Branches "1, 5, 9" as an example, the frequency components at $\omega_1 - \omega_2$ are shown as

$$p_{b1,5,9}|_{\omega=\omega 1-\omega 2} = \hat{p}_{\omega 1-\omega 2}\cdot\cos((\omega_1 - \omega_2)t + \delta - \theta) \tag{12}$$

where

$$\begin{aligned} &\hat{p}_{\omega 1-\omega 2} \\ &= \sqrt{\hat{v}_{m1}^2\hat{i}_{m2}^2 + \hat{v}_{m2}^2\hat{i}_{m1}^2 - 2\hat{v}_{m1}\hat{v}_{m2}\hat{i}_{m1}\hat{i}_{m2}\cos(\varphi - \theta)}/6 \\ &\delta = \operatorname{atan}(\hat{v}_{m1}\hat{i}_{m2}\sin\varphi/(\hat{v}_{m1}\hat{i}_{m2}\cos\varphi - \hat{v}_{m2}\hat{i}_{m1})). \end{aligned} \tag{13}$$

According to (14), when output frequency ω_2 gets close to the input frequency ω_1, the low-frequency power component at $\omega_1 - \omega_2$, shown in (12), will cause large branch energy fluctuation

$$|\Delta e_{bi}^{\omega}|_{\max} = \max\left(\int p_{bi}|_{\omega}\partial t\right) - \min\left(\int p_{bi}|_{\omega}\partial t\right) = 2\hat{p}_{\omega}/\omega. \tag{14}$$

When ω_1 is equal to ω_2, the low-frequency branch power components at $\omega_1 - \omega_2$ become nonzero constant so the capacitor voltages will diverge. As a result, when operates M3C around equal input and output frequencies, applying the basic branch current allocation makes the branch energy unstable. Therefore, the branch currents need to be reallocated.

III. Branch Energy Equilibrium Point of M3C When Operating Around Equal Frequency

A. Phasor Domain Analysis of the M3C

As explained in Section II, when the M3C operates with similar input and output frequencies, the basic branch current allocation is not the branch energy equilibrium point. In this section, an adjusted branch current allocation is developed to reestablish the branch energy equilibrium point. The analysis is performed in the phasor domain instead of time-domain. This assists in the visualization of the analysis of branch energy balancing. Rewriting the definitions of (8) to (10) in the phasor domain using the complex phasors given in (15)–(18). Phasors of ac grid voltages are as follows

$$\begin{aligned} &\vec{v}_{Gu} = \hat{v}_{m1},\ \vec{v}_{Gv} = \hat{v}_{m1}\cdot e^{j\cdot\alpha} \quad \vec{v}_{Gw} = \hat{v}_{m1}\cdot e^{j\cdot(-\alpha)} \\ &\alpha = -2\pi/3. \end{aligned} \tag{15}$$

Here, the real axis is in the same direction of phasor $\vec{v}_{Gu}$ and the imaginary axis is 90° ahead of the real axis. The phasors of input voltages and currents

$$\vec{v}_u = \hat{v}'_{m1}\cdot e^{j\cdot\gamma_1} \quad \vec{v}_v = \hat{v}'_{m1}\cdot e^{j\cdot(\alpha+\gamma_1)}\vec{v}_w = \hat{v}'_{m1}\cdot e^{j\cdot(-\alpha+\gamma_1)} \tag{16}$$

$$\vec{i}_u = \hat{i}_{m1} \quad \vec{i}_v = \hat{i}_{m1}\cdot e^{j\cdot\alpha} \quad \vec{i}_w = \hat{i}_{m1}\cdot e^{j\cdot(-\alpha)}. \tag{17}$$

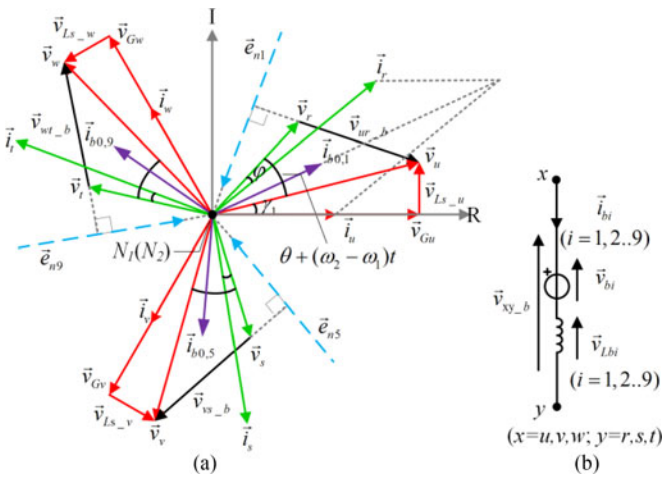

Fig. 3. Phasor diagram for the M3C. (a) Branches 1, 5, 9. (b) Phasors in a given branch.

Taking phase *r* as an example, phasors of output voltages and currents

$$\vec{v}_r = \hat{v}_{m2} \cdot e^{j\cdot((\omega_2-\omega_1)t+\theta+\gamma_1)} \quad \vec{i}_r = \hat{i}_{m2} \cdot e^{j\cdot((\omega_2-\omega_1)t+\theta-\varphi+\gamma_1)}. \tag{18}$$

In this paper, nine branches are symmetrically separated into three groups as Branches 1, 5, 9, Branches 2, 6, 7, and Branches 3, 4, 8. Taking Branches 1, 5, 9 as an example, the phasor diagram is shown in Fig. 3(a). In Fig. 3(a), the real axis and imaginary axis are denoted as "R" and "I," respectively. The ac grid voltages, input side voltages, and currents in (15) to (17) are shown in red; output side voltages, and currents in (18) are shown in green.

The phasors of the ac inductor voltages are defined as

$$\vec{v}_{Ls\_u} = j\omega_1 L_s \hat{i}_{m1} \quad \vec{v}_{Ls\_v} = j\omega_1 L_s \hat{i}_{m1} e^{j\alpha}$$
$$\vec{v}_{Ls\_w} = j\omega_1 L_s \hat{i}_{m1} e^{-j\alpha}. \tag{19}$$

$[\mathbf{v_{xy\_b}}]_{\mathbf{vec}}$ is the vector of branch voltages, $[\mathbf{v_b}]_{\mathbf{vec}}$ is the vector of the nine cascaded full-bridge output voltages, and $[\mathbf{v_{Lb}}]_{\mathbf{vec}}$ is the vector of the nine branch inductor voltages

$$[\mathbf{v_{xy\_b}}]_{\mathbf{vec}} = [\vec{v}_{ur\_b}\ \vec{v}_{us\_b}\ \vec{v}_{ut\_b}\ \vec{v}_{vr\_b}\ \vec{v}_{vs\_b}\ \vec{v}_{vt\_b}\ \vec{v}_{wr\_b}\ \vec{v}_{ws\_b}\ \vec{v}_{wt\_b}]^T$$
$$\vec{v}_{\mathbf{xy\_b}} = \vec{v}_x - \vec{v}_y \quad x = u,v,w \quad y = r,s,t \tag{20}$$
$$[\mathbf{v_b}]_{\mathbf{vec}} = [\vec{v}_{b1}\ \vec{v}_{b2}\ \vec{v}_{b3}\ \vec{v}_{b4}\ \vec{v}_{b5}\ \vec{v}_{b6}\ \vec{v}_{b7}\ \vec{v}_{b8}\ \vec{v}_{b9}]^T \tag{21}$$
$$[\mathbf{v_{Lb}}]_{\mathbf{vec}} = [\vec{v}_{Lb1}\ \vec{v}_{Lb2}\ \vec{v}_{Lb3}\ \vec{v}_{Lb4}\ \vec{v}_{Lb5}\ \vec{v}_{Lb6}\ \vec{v}_{Lb7}\ \vec{v}_{Lb8}\ \vec{v}_{Lb9}]^T. \tag{22}$$

The definition of phasors in $[\mathbf{v_{xy\_b}}]_{\mathbf{vec}}$, $[\mathbf{v_b}]_{\mathbf{vec}}$, and $[\mathbf{v_{Lb}}]_{\mathbf{vec}}$ is shown in Fig 3.(b). The three vectors satisfy

$$[\mathbf{v_{xy\_b}}]_{\mathbf{vec}} = [\mathbf{v}_b]_{\mathbf{vec}} + [\mathbf{v}_{Lb}]_{\mathbf{vec}}. \tag{23}$$

$[\mathbf{e_t}]_{\mathbf{vec}}$ is the vector of unit phasors on branch voltage directions. $[\mathbf{e_n}]_{\mathbf{vec}}$ is the vector of unit phasors perpendicular to $[\mathbf{e_t}]_{\mathbf{vec}}$ and it lags behind $[\mathbf{e_t}]_{\mathbf{vec}}$ 90°

$$[\mathbf{e_t}]_{\mathbf{vec}} = [\mathbf{k}]\,[\mathbf{v_{xy\_b}}]_{\mathbf{vec}} \quad [\mathbf{k}] = \begin{bmatrix} k_1 & & & \\ & k_2 & & \\ & & \ddots & \\ & & & k_9 \end{bmatrix} \quad k_i = \frac{1}{|\vec{v}_{\mathbf{xy\_b}}|} \tag{24}$$

$$[\mathbf{e_n}]_{\mathbf{vec}} = -j[\mathbf{e}_t]_{\mathbf{vec}} \quad [\mathbf{e_n}]_{\mathbf{vec}} = [\vec{e}_{n1}\ \vec{e}_{n2}\ \dots\ \vec{e}_{n9}]^T \quad \vec{e}_{ni} = e^{j\sigma_{bi}}. \tag{25}$$

According to (20), $[\mathbf{e_n}]_{\mathbf{vec}}$ can be separated into three groups and in each groups the phasors satisfy (26) to (28). In Fig. 3(a), phasors $\vec{e}_{ni}$ are shown in blue

$$[\mathbf{e_{n1,5,9}}]_{\mathbf{vec}} = [\vec{e}_{n1}\ \vec{e}_{n5}\ \vec{e}_{n9}] = [1\ e^{j\alpha}\ e^{j2\alpha}] \cdot \vec{e}_{n1} \tag{26}$$
$$[\mathbf{e_{n2,6,7}}]_{\mathbf{vec}} = [\vec{e}_{n2}\ \vec{e}_{n6}\ \vec{e}_{n7}] = [1\ e^{j\alpha}\ e^{j2\alpha}] \cdot \vec{e}_{n2} \tag{27}$$
$$[\mathbf{e_{n3,4,8}}]_{\mathbf{vec}} = [\vec{e}_{n3}\ \vec{e}_{n4}\ \vec{e}_{n8}] = [1\ e^{j\alpha}\ e^{j2\alpha}] \cdot \vec{e}_{n3}. \tag{28}$$

Similar to the idea in [25], to stabilize the branch energy in each branch the cascaded full-bridge output voltage $\vec{v}_{bi}$ needs to be perpendicular to the branch current $\vec{i}_{bi}$ ($\vec{i}_{bi} \perp \vec{v}_{bi}$). Obviously, on each branch, the branch inductor voltage $\vec{v}_{Lbi}$ is perpendicular to branch current $\vec{i}_{bi}$ ($\vec{i}_{bi} \perp \vec{v}_{Lbi}$). According to (23), to stabilize the branch energy the branch current $\vec{i}_{bi}$ should be perpendicular to the branch voltage $\vec{v}_{\mathbf{xy\_b}}$

$$\vec{i}_{bi} \perp \vec{v}_{\mathbf{xy\_b}} \quad (x = u,v,w \quad y = r,s,t \quad i = 1,2,\dots,9). \tag{29}$$

Combined with (24), (25), and (29), the branch currents should satisfy (30), where $c_i \in \Re \quad i = 1,2,\dots,9$. In each branch, the phasor $\vec{i}_{bi}$ needs to be in the same or opposite direction of $\vec{e}_{ni}$. In matrix **[C]**, c_1 to c_9 are the magnitude of nine branch currents. When $c_i > 0$, $\vec{i}_{bi}$ is in the same direction of $\vec{e}_{ni}$ and when $c_i < 0$, $\vec{i}_{bi}$ is in the opposite direction of $\vec{e}_{ni}$.

$$[\mathbf{i_b}]_{\mathbf{vec}} = [\mathbf{C}]\,[\mathbf{e_n}]_{\mathbf{vec}} \quad [\mathbf{i_b}]_{\mathbf{vec}} = [\vec{i}_{b1}\ \dots\ \vec{i}_{b9}]^T$$
$$[\mathbf{C}] = \begin{bmatrix} c_1 & & \\ & \ddots & \\ & & c_9 \end{bmatrix}. \tag{30}$$

Rewrite the definition of basic branch currents shown in (7) in phasor domain

$$\vec{i}_{b0,i} = (1/3)\cdot\vec{i}_x + (1/3)\cdot\vec{i}_y \quad i = 1,2,..9 \quad x = u,v,w$$
$$y = r,s,t. \tag{31}$$

In Fig. 3(a), the phasors of basic branch currents $\vec{i}_{b0,i}$ are shown in purple. There exist angle differences between the basic branch current phasors $\vec{i}_{b0,i}$ (i = 1,2,...,9) and $\vec{e}_{ni}$ (i = 1,2,...,9). The basic branch currents do not satisfy (30). Therefore, the basic branch current allocation will make the branch energy unstable, as predicted in Section II-C.

B. Branch Current Magnitude Calculation

Section II-A provided the method to calculate the phase angles of the adjusted branch currents in phasor domain. This

section provides a method to calculate the magnitudes of the nine adjusted branch currents. In the M3C, the branch currents should satisfy the constraints of (32)–(34) at the input side

$$\vec{i}_u = \vec{i}_{b1} + \vec{i}_{b2} + \vec{i}_{b3} = c_1 \cdot \vec{e}_{n1} + c_2 \cdot \vec{e}_{n2} + c_3 \cdot \vec{e}_{n3} \quad (32)$$

$$\vec{i}_v = \vec{i}_{b4} + \vec{i}_{b5} + \vec{i}_{b6} = c_4 \cdot \vec{e}_{n4} + c_5 \cdot \vec{e}_{n5} + c_6 \cdot \vec{e}_{n6} \quad (33)$$

$$\vec{i}_w = \vec{i}_{b7} + \vec{i}_{b8} + \vec{i}_{b9} = c_7 \cdot \vec{e}_{n7} + c_8 \cdot \vec{e}_{n8} + c_9 \cdot \vec{e}_{n9}. \quad (34)$$

Multiplying (33) by $e^{j\cdot 2\alpha}$ and (34) by $e^{j\cdot\alpha}$

$$\vec{i}_u = \vec{i}_v \cdot e^{j\cdot 2\alpha} = c_4 \cdot \vec{e}_{n3} + c_5 \cdot \vec{e}_{n1} + c_6 \cdot \vec{e}_{n2} \quad (35)$$

$$\vec{i}_u = \vec{i}_w \cdot e^{j\cdot\alpha} = c_7 \cdot \vec{e}_{n2} + c_8 \cdot \vec{e}_{n3} + c_9 \cdot \vec{e}_{n1}. \quad (36)$$

The current constraints (32)–(34) at the input side are equivalent to (32), (35), and (36). It can be proved that the magnitudes of branch currents c_i $(i = 1, 2, \ldots, 9)$ satisfy

$$c_1 = c_5 = c_9 \quad c_2 = c_6 = c_7 \quad c_3 = c_4 = c_8. \quad (37)$$

As a result, the branch current constraints at input side can be represented by a single constraint in (32). Similarly, the branch current constraints at the output side can be simplified as

$$\vec{i}_r = \vec{i}_{b1} + \vec{i}_{b4} + \vec{i}_{b7} = c_1 \cdot \vec{e}_{n1} + c_2 \cdot e^{j2\alpha} \cdot \vec{e}_{n2} + c_3 \cdot e^{j\alpha} \cdot \vec{e}_{n3}. \quad (38)$$

According to (32) and (38), the magnitudes of branch currents satisfy (39)–(41). The operator "Imag()" denotes the imaginary component of a phasor and the operator "Real()" denotes the real component of a phasor.

$$\mathrm{Imag}(c_1 \cdot \vec{e}_{n1} + c_2 \cdot \vec{e}_{n2} + c_3 \cdot \vec{e}_{n3}) = \mathrm{Imag}(\vec{i}_u) = 0 \quad (39)$$

$$\mathrm{Imag}(c_1 \cdot \vec{e}_{n1} + c_2 \cdot e^{j2\alpha} \cdot \vec{e}_{n2} + c_3 \cdot e^{j\alpha} \cdot \vec{e}_{n3}) = \mathrm{Imag}(\vec{i}_r) \quad (40)$$

$$\mathrm{Real}(c_1 \cdot \vec{e}_{n1} + c_2 \cdot e^{j2\alpha} \cdot \vec{e}_{n2} + c_3 \cdot e^{j\alpha} \cdot \vec{e}_{n3}) = \mathrm{Real}(\vec{i}_r). \quad (41)$$

As the real axis is on the same direction of phasor $\vec{v}_{Gu}$, the constraint in (39) ensures that there is no reactive power applied at the ac grid. Equations (40) and (41) ensure the current constraints at the output side. According to (39) to (41), the magnitudes of the branch currents can be calculated by solving the linear equations as

$$[\mathbf{A}]\begin{bmatrix} c_1 & c_2 & c_3 \end{bmatrix}^T = [\mathbf{B}] \quad (42)$$

where

$$[\mathbf{A}] = \begin{bmatrix} \sin\sigma_{b1} & \sin\sigma_{b2} & \sin\sigma_{b3} \\ \sin\sigma_{b1} & \sin(\sigma_{b2}+2\alpha) & \sin(\sigma_{b3}+\alpha) \\ \cos\sigma_{b1} & \cos(\sigma_{b2}+2\alpha) & \cos(\sigma_{b3}+\alpha) \end{bmatrix} \quad (43)$$

$$[\mathbf{B}] = \begin{bmatrix} 0 & \hat{i}_{m2}\cdot\sin(\theta-\varphi+\gamma_1) & \hat{i}_{m2}\cdot\cos(\theta-\varphi+\gamma_1) \end{bmatrix}^T. \quad (44)$$

With the calculated values of c_1, c_2, and c_3, the magnitude of the input currents $(\hat{i}_{m1})$ can be calculated by (32). Assuming $[c_1^* \; c_2^* \; c_3^*]^T$ is a possible solution of (42), combined with (30) and (37) the reallocated branch currents should be

$$[\mathbf{i_b}]^*_{\mathbf{vec}} = [\mathbf{C}]^*[\mathbf{e_n}]_{\mathbf{vec}} \quad [\mathbf{C}]^* = \begin{bmatrix} c_1^* & & \\ & \ddots & \\ & & c_9^* \end{bmatrix}, \begin{pmatrix} c_1^* = c_5^* = c_9^* \\ c_2^* = c_6^* = c_7^* \\ c_3^* = c_4^* = c_8^* \end{pmatrix}. \quad (45)$$

In this paper the reallocated branch currents $[\mathbf{i_b}]_{\mathbf{vec}} = [\mathbf{i_b}]^*_{\mathbf{vec}}$ are called the *branch energy equilibrium point* of M3C when operates with similar input and output frequencies.

C. Discussion on the Control Availability

As explained in Section I, the consideration in this paper is to equalize the energy of the nine branches by using only circulating currents in the M3C. According to the definition in (15) and (17), there is no reactive power at the input side. In Fig. 3(a), as the neutral point of the two three-phase systems (N_1 and N_2) are overlapped, there is also no common mode voltage injected. According to the analysis in Section III-B, if the matrix **[A]** is invertible, then the linear equation in (42) is solvable and the reallocated branch currents can be calculated. Defining the modulation rate *m* in (46), the determinant of the matrix **[A]** satisfies (47).

$$m = \hat{v}_{m2}/\hat{v}'_{m1} \geq 0 \quad (46)$$

$$\det([\mathbf{A}]) = 3\sqrt{3}(1-m^2)cos\gamma_1/2/\sqrt{m^2 - 2\cos\theta' m + 1}/\ldots \sqrt{m^2 + (\cos\theta' + \sqrt{3}\sin\theta')m + 1}/ \sqrt{m^2 + (\cos\theta' - \sqrt{3}\sin\theta')m + 1} \quad (47)$$

where

$$\theta' = (\omega_2 - \omega_1)\cdot t + \theta. \quad (48)$$

If $m \neq 1$, according to (47), the determinant of matrix **[A]** satisfies "det([A])≠0" so the matrix **[A]** is invertible, then as explained before the mentioned consideration is applicable and the magnitudes of the branch currents satisfies

$$[\,c_1^* \; c_2^* \; c_3^*\,]^T = [\mathbf{A}]^{-1}[\mathbf{B}] \quad c_1^* = c_5^* = c_9^* \quad c_2^* = c_6^* = c_7^* \quad c_3^* = c_4^* = c_8^*. \quad (49)$$

If $m = 1$, the matrix **[A]** is not invertible. To simplify the analysis, it is assumed that the input side frequency is equal to output frequency $(\omega_1 = \omega_2)$ and, therefore θ' in (48) is equal to θ

a. $m = 1$ $\theta = 0$ or $\theta = 2\pi/3$ or $\theta = -2\pi/3$

In these conditions, the vector of branch voltages $[\mathbf{v_{xy\_b}}]_{\mathbf{vec}}$ has zero components, so there is no definition of $[\mathbf{e_n}]_{\mathbf{vec}}$. The branch currents cannot be calculated using the method explained in Section III-B. If $\theta = 0$, input voltages and output voltages satisfy $\vec{v}_u = \vec{v}_r$, $\vec{v}_v = \vec{v}_s$, $\vec{v}_w = \vec{v}_t$. In this case, the power transfer from input side to output side can be realized by controlling the cascaded full-bridges in Branches 1, 5, 9 to output zero voltage and blocking the cascaded full-bridges in Branches 2, 6, 7 and Branches 3, 4, 8. Similarly, the control for $\theta = 2\pi/3$ and $\theta = -2\pi/3$ are shown in Table I. However, the load needs to be purely resistive to ensure no reactive power at the ac grid

TABLE I
OPERATION METHOD FOR THREE SPECIAL CONDITIONS

$m=1$	Branches 1, 5, 9	Branches 2, 6, 7	Branches 3, 4, 8
$\theta=0$	$*$	Blocked	Blocked
$\theta=2\pi/3$	Blocked	$*$	Blocked
$\theta=-2\pi/3$	Blocked	Blocked	$*$

'$*$': The output voltage of the cascaded full-bridges is zero.

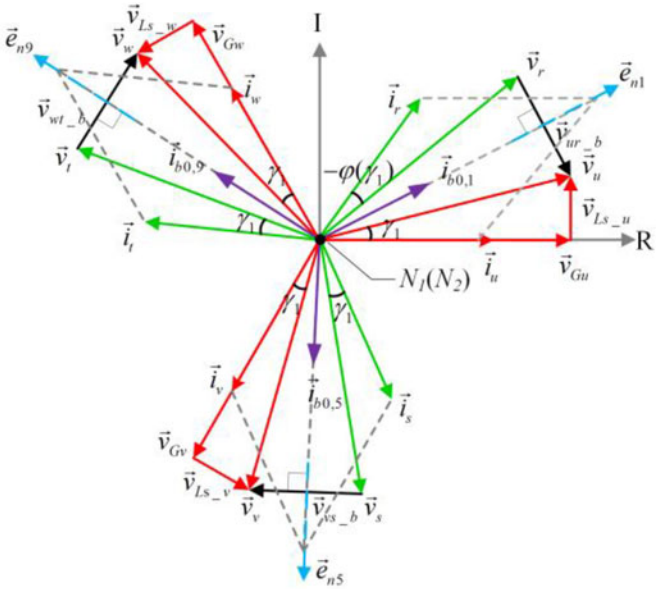

Fig. 4. Phasor diagram on the condition of "$\gamma_1=-\varphi$."

b. $m=1$ $\theta\neq 0, 2\pi/3, -2\pi/3$

When $m=1$, the determinant of matrix **[A]** equals to zero. The rank of matrix **[A]** is smaller than 2 ($\mathrm{rank}([\mathbf{A}])\leq 2$). Assuming $[\mathbf{A}]=[\,\mathbf{a_1}\ \mathbf{a_2}\ \mathbf{a_3}\,]$, where $\mathbf{a}_1$, $\mathbf{a}_2$, and $\mathbf{a}_3$ are column blocks of matrix A. If the linear equation in (42) has a solution, the rank of matrix **[A B]** satisfies

$$\mathrm{rank}([\,\mathbf{A}\ \mathbf{B}\,])=\mathrm{rank}([\mathbf{A}])\leq 2\Rightarrow\begin{cases}\det([\,\mathbf{a_1}\ \mathbf{a_2}\ \mathbf{B}\,])=0\\ \det([\,\mathbf{a_1}\ \mathbf{a_3}\ \mathbf{B}\,])=0\\ \det([\,\mathbf{a_2}\ \mathbf{a_3}\ \mathbf{B}\,])=0\end{cases}. \tag{50}$$

Taking matrix $[\mathbf{a_1}\ \mathbf{a_2}\ \mathbf{B}]$ as an example, its determinant satisfies (51). It can be proved that the linear equations in (42) has solutions only if condition (52) is met. Since $\gamma_1\approx 0$, the power factor angle at the output side is almost zero (the load is almost purely resistive). In the condition of (52), the basic branch currents are one of the solutions for the linear equations in (42). Taking Branches 1, 5, 9 as an example, the phasor diagram is shown in Fig. 4. As the basic branch currents are in the same direction as $[\mathbf{en}]_{\mathbf{vec}}$, there is no active power on each branch and the branch energy is stabilized

$$\det([\mathbf{a_1}\ \mathbf{a_2}\ \mathbf{B}])=-\frac{\sqrt{3}\hat{i}_{2m}\left(2\cos(\theta-\pi/3)-1\right)\sin(\gamma_1+\varphi)}{4\sqrt{1-\cos\theta}\cdot\sqrt{1+\cos(\theta+\pi/3)}}$$
$$=0 \tag{51}$$

$$\sin(\gamma_1+\varphi)=0\Rightarrow\gamma_1=-\varphi. \tag{52}$$

In conclusion, when magnitudes of input and output voltages are not the same ($m\neq 1$), it is possible to stabilize the branch energy by using only circulating currents in the M3C. However, when $m=1$, the allocation is only possible when the load is purely resistive. Otherwise, the common-mode voltage or reactive power at the ac grid side is required.

D. Adjusted Branch Power

According to the analysis in Section III-C, when the modulation rate $m\neq 1$, the matrix **[A]** is invertible and the solution of (42) can be calculated as **[A]$^{-1}$[B]**. According to (24), (25), and (30), the branch currents satisfy

$$[\mathbf{i_b}]_{\mathbf{vec}}=(-j)\cdot[\mathbf{C}]\cdot[\mathbf{k}]\cdot[\mathbf{v_{xy\_b}}]_{\mathbf{vec}}. \tag{53}$$

Taking Branch 1 as an example, the voltage and current phasors in Branch 1 satisfy (54). The branch power on Branch 1 then satisfies (55), where $d=(1-\omega_2 L_b c_1 k_1)\cdot c_1 k_1/2$. Similarly, all the branch powers can be calculated. Branches "1, 5, 9," "2, 6, 7," or "3, 4, 8" share a same branch power respectively ($p_{b1}=p_{b5}=p_{b9}$, $p_{b2}=p_{b6}=p_{b7}$, $p_{b3}=p_{b4}=p_{b8}$) Compared to the branch power under the basic current allocations in (11) there is no frequency component ω_1-ω_2. As a result, using the reallocated branch currents can make the branch energy stable when the M3C is operated with similar input and output frequencies

$$\vec{v}_{b1}=\vec{v}_u-\vec{v}_r-j\omega_2 L_b\vec{i}_{b1}\quad \vec{i}_{b1}=-j\cdot c_1\cdot k_1\cdot(\vec{v}_u-\vec{v}_r) \tag{54}$$

$$p_{b1}=v_{b1}i_{b1}=\mathrm{Real}(\vec{v}_{b1})\cdot\mathrm{Real}(\vec{i}_{b1})=d\hat{v}_{m1}^{\prime 2}\sin(2\omega_1 t+2\gamma_1)$$
$$+\ldots d\hat{v}_{m2}^{2}\sin(2\omega_2 t+2\theta+2\gamma_1)$$
$$-2d\hat{v}^{\prime}_{m1}\hat{v}_{m2}\sin((\omega_1+\omega_2)t+\theta+2\gamma_1). \tag{55}$$

IV. BRANCH-BALANCING CONTROL METHOD

A. Branch Current Reallocation Strategy

According to the analysis in Section III, if the voltage magnitude at the input side and output side are not identical, the reallocated branch currents defined in (45) and (49) can be applied to suppress the capacitor-voltage fluctuation when output frequency gets close to the input frequency. In this section, the theoretical calculation process in the phasor domain explained in Section III is used as a real-time control method. The control block is shown in Fig. 5. Generally, *there are four steps to get the reallocated branch currents* in the proposed branch current reallocation method: Step 1. Calculating phasors $\vec{e}_{ni}(i=1,2,\ldots,9)$; Step 2. Adjusting phase angles of $\vec{e}_{ni}$ according to capacitor voltage differences; Step 3. Calculating branch current magnitudes $c_i(i=1,2,\ldots,9)$ by solving linear equations $[\mathbf{A}][\,c_1\ c_2\ c_3\,]^T=[\mathbf{B}]$; Step 4. Getting the reallocated branch currents. These steps are marked in Fig. 5.

In Fig. 5, $v_\alpha^{uvw}, v_\beta^{uvw}$ are the input side voltage references on $\alpha\beta$ frames and $v_\alpha^{rst}, v_\beta^{rst}$ are the output side voltage references on $\alpha\beta$ frames. Currents i_r, i_s, i_t are the measured three-phase load currents. Using Clarke transformation to get the magnitudes and angles of phasors $\vec{v}_u$, $\vec{v}_r$, and $\vec{i}_r$ as "$\hat{v}^{\prime}_{m1}$, θ_1," "$\hat{v}_{m2}$, θ_2,"

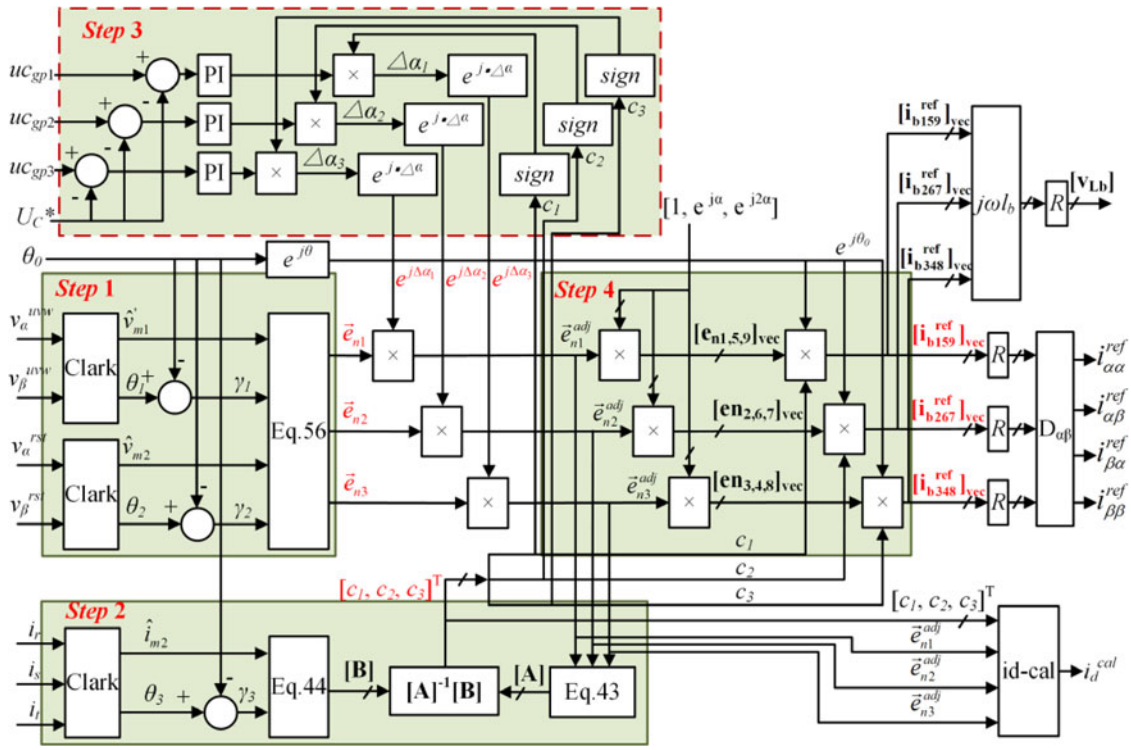

Fig. 5. Proposed branch current reallocation strategy.

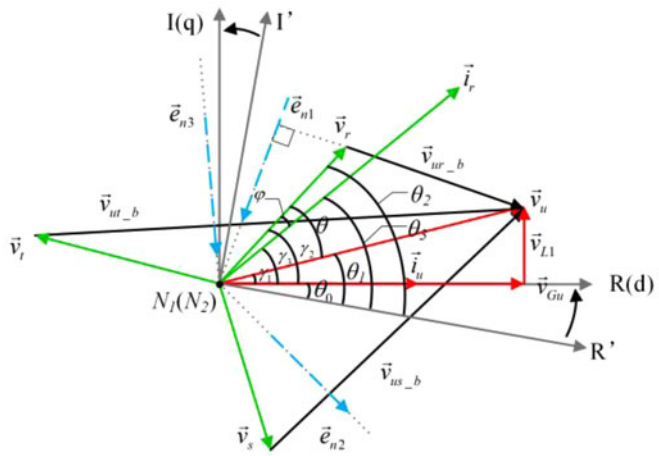

Fig. 6. Angle definitions in the proposed control.

and "$\hat{i}_{m2}$, θ_3." The angle definitions are shown in Fig. 6. θ_0 is the angle of phasor $\vec{v}_{Gu}$ which can be calculated from phase-locked loops. There exist an angle difference between phasor $\vec{v}_{Gu}$ and the real-axis R' shown in Fig. 6. To coincide with the phasor definitions in Section III, the real axis is moved to the direction of $\vec{v}_{Gu}$. Subtracted by θ_0, the angle of $\vec{v}_u$, $\vec{v}_r$, and $\vec{i}_r$ are denoted as γ_1, γ_2, and γ_3.

According to (24) and (25), phasors $\vec{e}_{n1}$, $\vec{e}_{n2}$, and $\vec{e}_{n3}$ can be calculated by (56). Theoretically the calculated $\vec{e}_{n1}$, $\vec{e}_{n2}$, and $\vec{e}_{n3}$ are absolutely perpendicular to $\vec{v}_{b1}$, $\vec{v}_{b2}$, and $\vec{v}_{b3}$, so there is no active power in each branch. However, due to measurement and small calculation errors, the calculated $\vec{e}_{n1}$, $\vec{e}_{n2}$, and $\vec{e}_{n3}$ have angle errors. Since $\vec{e}_{n5}$ to $\vec{e}_{n9}$ are calculated by using (26)–(28), the angle error has a similar effect on Branches 1, 5, 9, as it does on Branches 2, 6, 7 and on Branches 3, 4, 8. Denoting Branches "1, 5, 9," "2, 6, 7," and '3, 4, 8' as Branch Groups 1, 2, and 3, the group capacitor voltages are defined in (57), where u_{ci}^{avg} $(i = 1, \ldots, 9)$ is the average capacitor voltage in a given branch

$$\vec{e}_{n1} = -j\frac{\vec{v}_u - \vec{v}_r}{|\vec{v}_u - \vec{v}_r|} \quad \vec{e}_{n2} = -j\frac{\vec{v}_u - \vec{v}_s}{|\vec{v}_u - \vec{v}_s|} \quad \vec{e}_{n3} = -j\frac{\vec{v}_u - \vec{v}_t}{|\vec{v}_u - \vec{v}_t|} \tag{56}$$

$$uc_{gp1} = \sum_{i=1,5,9} u_{ci}^{\text{avg}}/3 \quad uc_{gp2} = \sum_{i=2,6,7} u_{ci}^{\text{avg}}/3$$
$$uc_{gp3} = \sum_{i=3,4,8} u_{ci}^{\text{avg}}/3. \tag{57}$$

The angle errors of $\vec{e}_{n1}$, $\vec{e}_{n2}$, and $\vec{e}_{n3}$ cause an energy difference among Branch Groups 1, 2, and 3. The phase angles of $\vec{e}_{n1}$, $\vec{e}_{n2}$, and $\vec{e}_{n3}$ need to be adjusted to regulate the branch energy. For instance if the group capacitor voltages satisfy $uc_{gp1} < U_c*$, $uc_{gp2} > U_c*$, $uc_{gp3} > U_c*$ (U_c* is the reference capacitor voltage) and the calculated branch current magnitudes satisfy $c_1 > 0$, $c_2 > 0$, $c_3 < 0$, the regulation process is shown in Fig. 7. In Branch Group 1, because $uc_{gp1} < U_c*$, an extra positive active power need to be supplemented, so the phasor of the branch reference current needs to be moved closer to the phasor of the branch voltage with an angle of $\triangle\alpha_1$. Since $c_1 > 0$, the adjusted $\vec{e}_{n1}^{\text{adj}}$ is shown in Fig. 7(a). In Branch Group 2, because $uc_{gp2} > U_c*$, an extra negative active power need to be supplemented, so the branch reference current needs to be moved away from branch voltage with an angle of $\triangle\alpha_2$. Since

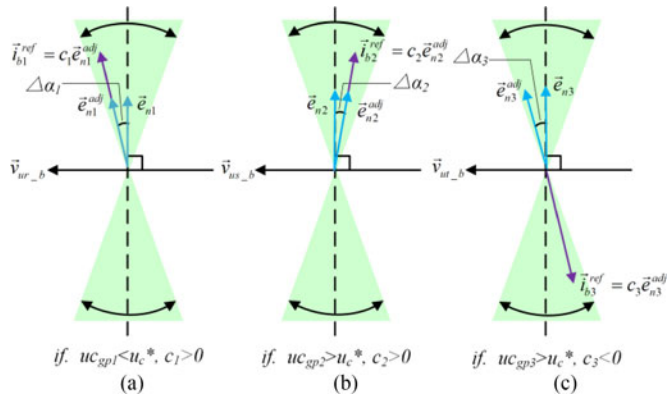

Fig. 7. Slight adjustments of $\vec{e}_{n1}$, $\vec{e}_{n2}$, and $\vec{e}_{n3}$. (a) Branch Group 1. (b) Branch Group 2. (c) Branch Group 3.

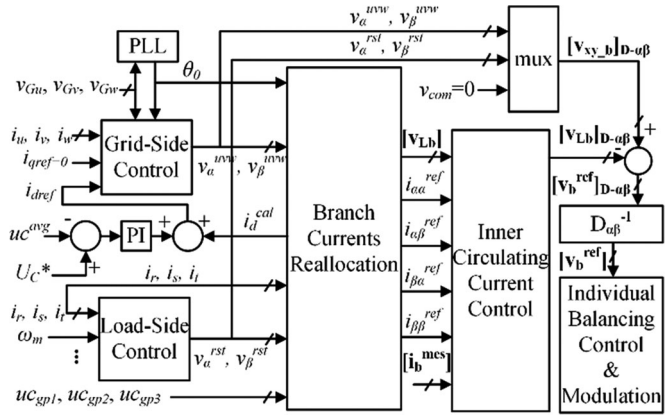

Fig. 8. Overall control strategy for the M3C.

$c_2 > 0$, the adjusted $\vec{e}_{n2}^{\,\mathrm{adj}}$ is shown in Fig. 7(b). In Branch Group 3, because $uc_{gp3} > U_c*$, an extra negative active power need to be supplemented, so the branch reference current needs to be moved away from branch voltage with an angle of $\triangle\alpha_3$. Since $c_3 < 0$, the adjusted $\vec{e}_{n3}^{\,\mathrm{adj}}$ is in the opposite direction of the branch current shown in Fig. 7(c). The angle of $\triangle\alpha_1$, $\triangle\alpha_2$, and $\triangle\alpha_3$ can be calculated by proportional-integral (PI) controller shown in dashed line box in Fig. 5.

With the adjusted $\vec{e}_{n1}^{\,\mathrm{adj}}$, $\vec{e}_{n2}^{\,\mathrm{adj}}$, and $\vec{e}_{n3}^{\,\mathrm{adj}}$, the matrix **[A]** is calculated according to (43). Matrix **[B]** can be calculated according to (44). Branch currents magnitude c_1, c_2, and c_3 are calculated by $\mathbf{[A]^{-1}[B]}$. The three groups of $[\mathbf{e_{n1,5,9}}]_{\mathbf{vec}}$, $[\mathbf{e_{n2,6,7}}]_{\mathbf{vec}}$, and $[\mathbf{e_{n3,4,8}}]_{\mathbf{vec}}$ are calculated according to (26) to (28). The nine branch currents satisfy

$$\begin{cases} [\mathbf{i^{ref}_{b159}}]_{\mathbf{vec}} = \begin{bmatrix} \vec{i}_{b1}^{\,ref} & \vec{i}_{b5}^{\,ref} & \vec{i}_{b9}^{\,ref} \end{bmatrix}^T = c_1 [\mathbf{e_{n1,5,9}}]_{\mathbf{vec}} e^{j\theta_0} \\ [\mathbf{i^{ref}_{b267}}]_{\mathbf{vec}} = \begin{bmatrix} \vec{i}_{b2}^{\,ref} & \vec{i}_{b6}^{\,ref} & \vec{i}_{b7}^{\,ref} \end{bmatrix}^T = c_2 [\mathbf{e_{n2,6,7}}]_{\mathbf{vec}} e^{j\theta_0} \\ [\mathbf{i^{ref}_{b348}}]_{\mathbf{vec}} = \begin{bmatrix} \vec{i}_{b3}^{\,ref} & \vec{i}_{b4}^{\,ref} & \vec{i}_{b8}^{\,ref} \end{bmatrix}^T = c_3 [\mathbf{e_{n3,4,8}}]_{\mathbf{vec}} e^{j\theta_0} \end{cases} . \tag{58}$$

However, a direct application of these currents will possibly influence input and output side three-phase currents. To avoid this effect, in Fig. 5 a Dual-$\alpha\beta$ transformation is performed and branch current references are applied as circulating currents. Because of the decoupling of the Dual-$\alpha\beta$ transformation, the effect on input and output side three-phase currents can then be eliminated. The introduction of the Dual-$\alpha\beta$ transformation might affect the capacitor voltage balancing but since the phase angle adjustment is very small as shown in Fig. 7, these effects can be neglected in practice. The input side current magnitude $\hat{i}_{m1}$ can be calculated using (59). It is also the d-axis current reference value for the grid side control under d-q frame. The instantaneous voltage drop on branch inductors can be calculated as (60)

$$i_d^{\mathrm{cal}} = \hat{i}_{m1} = \mathrm{Real}(c_1 \cdot \vec{e}_{n1}^{\,\mathrm{adj}} + c_2 \cdot \vec{e}_{n2}^{\,\mathrm{adj}} + c_3 \cdot \vec{e}_{n3}^{\,\mathrm{adj}}) \tag{59}$$

$$[\mathbf{v}_{Lb}] = \begin{bmatrix} v_{Lb1} & v_{Lb2} & v_{Lb3} \\ v_{Lb4} & v_{Lb5} & v_{Lb6} \\ v_{Lb7} & v_{Lb8} & v_{Lb9} \end{bmatrix} = \mathrm{Real}\left(j\omega L_b \begin{bmatrix} \vec{i}_{b1}^{\,\mathrm{ref}} & \vec{i}_{b2}^{\,\mathrm{ref}} & \vec{i}_{b3}^{\,\mathrm{ref}} \\ \vec{i}_{b4}^{\,\mathrm{ref}} & \vec{i}_{b5}^{\,\mathrm{ref}} & \vec{i}_{b6}^{\,\mathrm{ref}} \\ \vec{i}_{b7}^{\,\mathrm{ref}} & \vec{i}_{b8}^{\,\mathrm{ref}} & \vec{i}_{b9}^{\,\mathrm{ref}} \end{bmatrix} \right). \tag{60}$$

B. Overall Control Strategy for the M3C

For the M3C topology the capacitor-voltage balancing control consists of three levels [5]:

1) *overall-balancing control* regulates the average value of all capacitor voltages to the voltage command;
2) *branch-balancing control* regulates the average value of capacitor voltages among the nine branches;
3) *individual-balancing control* regulates the value of capacitor voltages of different full-bridge converter cells in each branch.

Correspondingly, the overall control strategy for the M3C consists of four modules, grid-side control, load-side control, branch-balancing control, and individual-balancing control. The overall control block is shown in Fig. 8.

The grid-side control realizes the overall-balancing control. It adjusts the active power on the input side to regulate the total energy stored in all nine branches and ensure unity power factor at ac grid. In this paper, a traditional d-q frame-based grid-connect control method is applied [26]. The current reference value in q-axis is set to be zero. The branch current reallocation strategy, as explained in Section IV-A, provides a calculated current reference value on d-axis (i_d^{cal}) in (59). To avoid the effects of calculation or measurement errors, the reference values are adjusted by a PI regulator. The PI regulator adjusts i_d^{ref} from i_d^{cal} according to the total capacitor voltage deviation. As shown in Fig. 8, uc^{avg} is the average capacitor voltage of all the full-bridge cells in the M3C. The grid-side control finally provides the M3C input side voltage references v_α^{uvw} and v_β^{uvw}. The load-side control realizes the regulation of machine speed, torque or so on. The load-side control provides the M3C output side voltage references v_α^{rst} and v_β^{rst}.

In Fig. 8, the branch-balancing control regulates the average capacitor voltages among the nine branches by the reallocation of the branch currents. The branch current reallocation strategy, explained in Section IV-A, provides the calculated branch inductor voltages $[\mathbf{v_{Lb}}]$ and the reference circulating currents $i_{\alpha\alpha}^{ref}$, $i_{\alpha\beta}^{ref}$, $i_{\beta\alpha}^{ref}$, $i_{\beta\beta}^{ref}$. Applying a double $\alpha\beta$ transformation on $[\mathbf{v_{Lb}}]$, the transformed branch inductor voltages are shown in (61). To realize accurate control of the four circulating currents, according to the equivalent circuits shown in Fig. 2, the

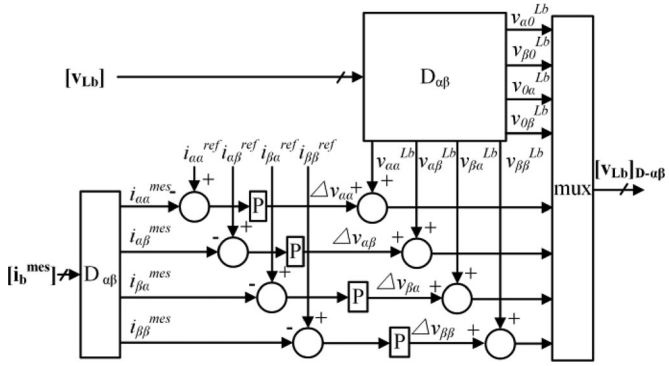

Fig. 9. Inner circulating current control.

branch inductor voltages $v_{\alpha\alpha}^{Lb}$, $v_{\alpha\beta}^{Lb}$, $v_{\beta\alpha}^{Lb}$, $v_{\beta\beta}^{Lb}$ need to be regulated. The regulation, as shown in Fig. 9, is realized using proportional regulators according to the error between the measured ($i_{\alpha\alpha}^{mes}$, $i_{\alpha\beta}^{mes}$, $i_{\beta\alpha}^{mes}$, i_{β}^{mes}) and the reference circulating current values ($i_{\alpha\alpha}^{ref}$, $i_{\alpha\beta}^{ref}$, $i_{\beta\alpha}^{ref}$, $i_{\beta\beta}^{ref}$)

$$\mathbf{T}_{Dual-\alpha\beta}([\mathbf{v}_{Lb}]) = \begin{bmatrix} v_{\alpha\alpha}{}^{Lb} & v_{\alpha\beta}{}^{Lb} & v_{\alpha 0}{}^{Lb} \\ v_{\beta\alpha}{}^{Lb} & v_{\beta\beta}{}^{Lb} & v_{\beta 0}{}^{Lb} \\ v_{0\alpha}{}^{Lb} & v_{0\beta}{}^{Lb} & v_{00}{}^{Lb} \end{bmatrix}. \quad (61)$$

In Fig. 8, $[\mathbf{v_{xy\_b}}]_{\mathbf{D-\alpha\beta}}$ defined in (5) is the matrix of branch voltages in double $\alpha\beta$ frames. In $[\mathbf{v_{xy\_b}}]_{\mathbf{D-\alpha\beta}}$, the common mode voltage v_{com} is set to be zero. As a result, the output voltage references of the nine cascaded full-bridges are equal to the difference between branch voltages and the branch inductor voltages as in (62). The individual-balancing control and the modulations on converter cells are then performed based on these voltage references

$$\begin{aligned}[\mathbf{v}_b{}^{\mathbf{ref}}] &= [\mathbf{v_{xy\_b}}]_{D-\alpha\beta} - [\mathbf{v}_{Lb}]_{D-\alpha\beta} \\ &= \begin{bmatrix} 0 & 0 & v_\alpha^{uvw} \\ 0 & 0 & v_\beta^{uvw} \\ -v_\alpha^{rst} & -v_\beta^{rst} & 0 \end{bmatrix} - \left(\begin{bmatrix} v_{\alpha\alpha}{}^{Lb} & v_{\alpha\beta}{}^{Lb} & v_{\alpha 0}{}^{Lb} \\ v_{\beta\alpha}{}^{Lb} & v_{\beta\beta}{}^{Lb} & v_{\beta 0}{}^{Lb} \\ v_{0\alpha}{}^{Lb} & v_{0\beta}{}^{Lb} & v_{00}{}^{Lb} \end{bmatrix} \right. \\ &\quad \left. + \begin{bmatrix} \Delta v_{\alpha\alpha} & \Delta v_{\alpha\beta} & 0 \\ \Delta v_{\beta\alpha} & \Delta v_{\beta\beta} & 0 \\ 0 & 0 & 0 \end{bmatrix} \right). \end{aligned} \quad (62)$$

Individual-balancing control balances the value of capacitor voltages of different full-bridge cells in each branch. This can be achieved by many well-constructed methods like capacitor voltage sorting based on phase-disposition carrier pulse-width modulation (PD-PWM) [8] or reference voltage adjustment for each full-bridge based on phase-shift carrier PWM (PS-PWM) [27].

C. Control Limitation Considering the Increased Current Stress

Under the basic branch current allocation, each branch consists of 1/3 of the *x*-phase ($x = u,v,w$) input side current and 1/3 of the *y*-phase ($y = r,s,t$) output side current. In this condition,

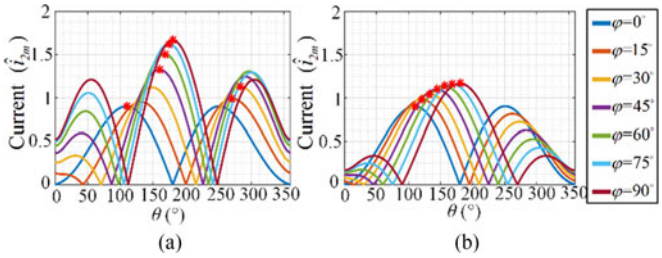

Fig. 10. Current stresses on Branches 1, 5, 9 when $m = 0.75$. (a) Using the proposed control method. (b) Using the control scheme in [4].

the maximum branch current stress I_{MAX} satisfies

$$I_{\mathrm{MAX}} = (\hat{i}_{m1} + \hat{i}_{m2})/3. \quad (63)$$

Neglecting the effect of the ac inductor L_s, based on the analysis in Section II, taking Branch 1 as an example, the calculated branch current magnitudes are

$$c_1 = (2\cos\varphi \cdot \sin(\theta) \cdot m^2 + \sin\varphi \cdot m + 2\sin(\varphi - \theta)) \cdot \ldots \sqrt{m^2 - 2\cos(\theta) \cdot m + 1} \cdot \hat{i}_{2m}/3/(1 - m^2). \quad (64)$$

Defining the nine branch current stresses as $\hat{i}_{bmi}$ (i = 1,2,...,9) in (65), where "Abs" is the absolute value function. For a fixed modulation rate m and a fixed load current magnitude $\hat{i}_{m2}$, the branch current stresses are functions of angle difference θ and load power factor angle φ. Fig. 10 (a) illustrates the current stresses on Branches 1, 5, 9 when modulation rate and load current magnitude are set as 0.75 and 1. Clearly, the larger the reactive power is at the output side, the larger the possible maximum current stress is on the branch (shown in red star)

$$\hat{i}_{bm1,5,9} = \mathrm{Abs}(c_1)\ \ \hat{i}_{bm2,6,7} = \mathrm{Abs}(c_2)\ \ \hat{i}_{bm3,4,8} = \mathrm{Abs}(c_3). \quad (65)$$

The control scheme in [4] injects circulating currents on the condition that the input and output side three-phase systems share an opposite value of reactive power. Using the proposed method in this paper, we can also get the branch current allocation under this condition. According to (39), we only need to change the first element in vector **[B]** from 0 to "$\hat{i}_{m1}\sin\varphi$" since the imaginary part of $\vec{i}_u$ has changed. The vector **[B]** in (44) changes to

$$[\mathbf{B}] = [\hat{i}_{m1}\sin\varphi\ \hat{i}_{m2}\sin(\theta - \varphi + \gamma_1)\ \hat{i}_{m2}\cos(\theta - \varphi + \gamma_1)]^T. \quad (66)$$

Neglecting ac inductor L_s, by solving the linear equation in (42), the branch current magnitude on branch 1, 5, 9 is

$$c_1{}' = \sqrt{m^2 - 2\cos(\theta) \cdot m + 1} \cdot 2\sin(\varphi - \theta) \cdot \hat{i}_{2m}/3. \quad (67)$$

Obviously, the value of (64) and (67) is the same when the load is pure resistive (φ= 0). Fig. 10 gives the numerical comparison between the proposed control and the control scheme in [4] in terms branch current stresses. In Fig. 10, at the extreme condition (φ= 90°) the branch current stress is 30% higher than the branch stress in [4] but the benefit is that there is no reactive power at the grid side. In addition, it is convenient to set an adjustment

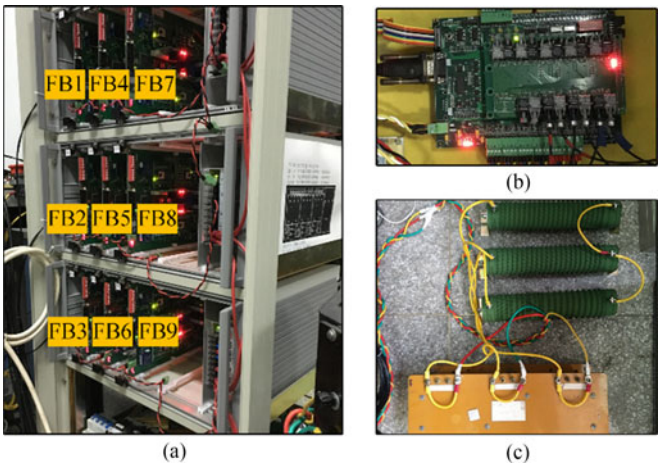

Fig. 11. M3C Experiment Platform. (a) M3C main circuit. (b) Central ciontroller. (c) *R–L* load.

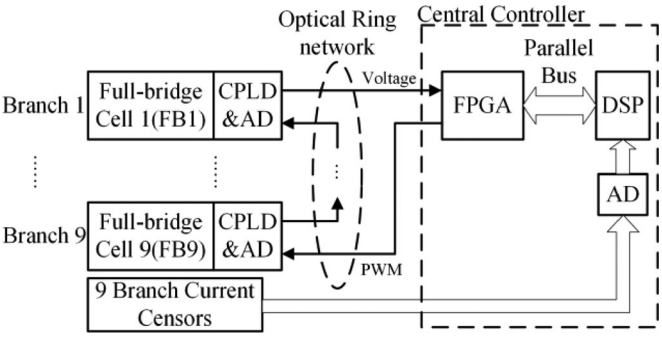

Fig. 12. Control system of the prototype.

factor ξ at the first element of vector **[B]** as

$$[\mathbf{B}] = \left[\xi \cdot \hat{i}_{m1} \sin\varphi \hat{i}_{m2} \sin(\theta - \varphi + \gamma_1) \hat{i}_{m2} \cos(\theta - \varphi + \gamma_1)\right]^T. \tag{68}$$

Future researches will focus on the adjustment of ξ to get an optimized compromise between the reactive power at the grid side and the limitation of branch current stresses.

V. Experiment Results

A. System Configuration and Capacitor Voltage Balancing Verification

A low-power M3C prototype is build up to validate the proposed analysis and control strategy. The research in this paper focuses on the branch-balancing control of the M3C. Therefore, to simplify the platform and control, the individual-balancing control is simplified by using only one full-bridge cell in each branch. The experiment platform is shown in Fig. 11. Fig. 12 shows the control system of the prototype. It consists of a central controller and nine full-bridge cells. The central controller uses a 32-b floating-point digital signal processor TMS320F28377 and a field-programmable gate array. Each full-bridge cell has a cell controller based on a complex programmable logic device. Central controller and cell controllers are connected in an optical ring network. PWM signals and capacitor voltages are transmitted through this network.

TABLE II
Experiment Parameters

Parameters	Symbols	Value
Switching Frequency	f_s	2 kHz
Full-bridge cells per branch	N	1
Module Capacitance	C	880 uF
Branch inductance	L_b	2 mH
AC grid inductance	L_s	5 mH
Capacitor Voltage	U_C*	150 V
Input frequency	f_1	50 Hz
Input Voltage Magnitude	$\hat{v}_{m\,1}$	80 V
Output Voltage Magnitude	$\hat{v}_{m\,2}$	60 V
Load Resistance	R	5 Ω
Load Reluctance	L	0 or 10 mH

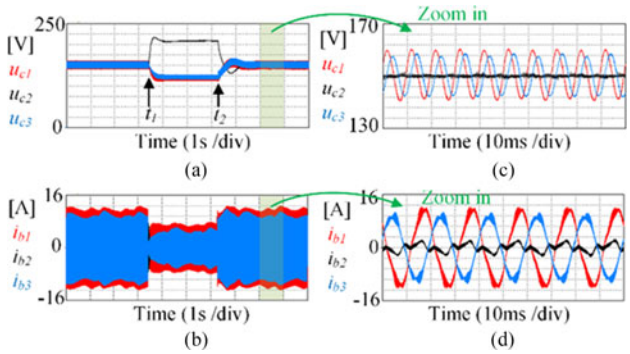

Fig. 13. Capacitor voltages balancing with $R = 5\ \Omega$ and $L = 0$, $\theta = 120°$. (a) Capacitor voltages. (b) Branch currents. (c) Zoomed-in capacitor voltages. (d) Zoomed-in branch currents.

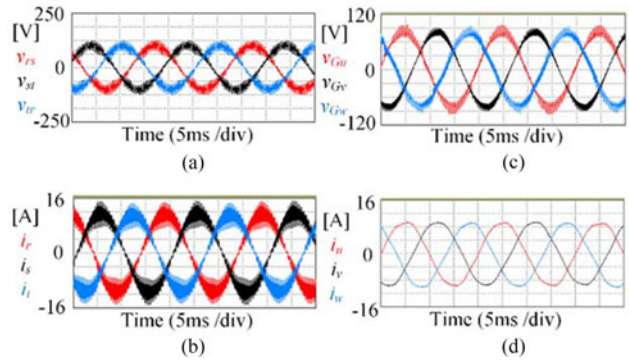

Fig. 14. Capacitor voltages balancing with $R = 5\ \Omega$ and $L = 0$, $\theta = 120°$. (a) Output line-to-line voltages. (b) Output currents. (c) AC grid phase-to-neutral voltages. (d) Input currents.

Table II summarizes the circuit parameters used for the experiment. The reference voltage of each module capacitor is set as $U_C{}^* = 150$ V.

Figs. 13 and 14 show the experimental results of the prototype with output fundamental frequency $f_2 = 50$ Hz, load resistance $R = 5\ \Omega$, and load reluctance $L = 0$, $\theta = 120°$. Fig. 13(a) and (b) shows the capacitor voltages and branch currents of Branchs 1, 2, and 3. Before time t_1, the proposed branch-balancing method is applied. Capacitor voltages coincide to each other and fluctuate around 150 V. At time t_1, the basic branch current allocation is applied instead. The capacitor voltages become unbalanced

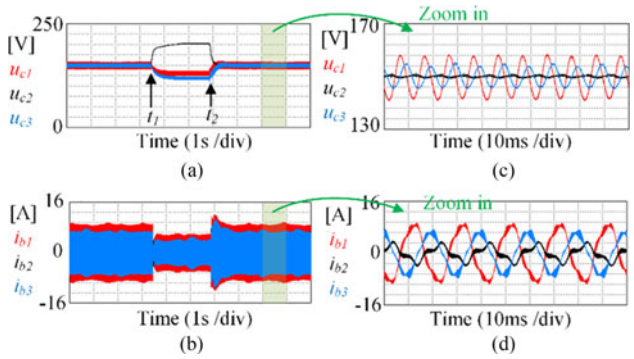

Fig. 15. Capacitor voltages balancing with $R = 5\ \Omega$ and $L = 10$ mH, $\theta = 150°$. (a) Capacitor voltages. (b) Branch currents. (c) Zoomed-in capacitor voltages. (d) Zoomed-in branch currents.

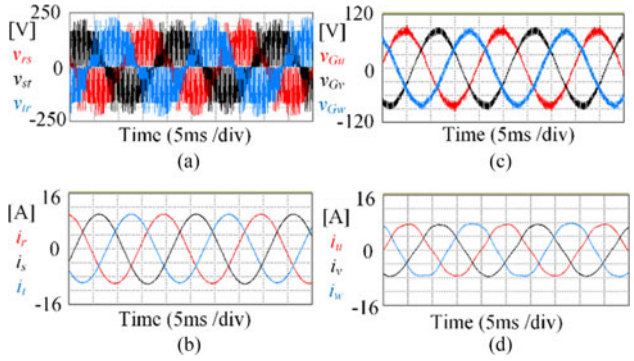

Fig. 16. Capacitor voltages balancing with $R = 5\ \Omega$ and $L = 10$ mH, $\theta = 150°$. (a) Output line-to-line voltages. (b) Output currents. (c) AC grid phase-to-neutral voltages. (d) Input currents.

quickly. This consists with the analysis before. At time t_2, the proposed control is applied again and the capacitor voltages become balanced again. Fig. 13(c) and (d) are the zoom-in results of Fig. 13(a) and (b) in steady state. It can be seen that the capacitor voltages are stabilized and balanced very well. In addition, there is a number of harmonics in $i_{\mathrm{b}1}$, $i_{\mathrm{b}2}$, and $i_{\mathrm{b}3}$. It is because $\vec{e}_{ni}(i = 1, 2, 3)$ need to be adjusted according to the branch energy differences as shown in Fig. 7. These adjustments will make the direction of $\vec{e}_{ni}(i = 1, 2, 3)$ changes and result in some harmonics in branch currents.

Fig. 14 shows the output line-to-line voltages v_{rs}, v_{st}, v_{tr}, output currents i_r, i_s, i_t, ac grid voltages v_{Gu}, v_{Gv}, v_{Gw}, and input currents i_u, i_v, i_w. As the ac grid voltages are in phase with the input currents, there is no reactive power applied at the ac grid.

A similar verification is also applied for an inductive load. The output fundamental frequency $f_2 = 50$ Hz and load resistance $R = 5\ \Omega$, load reluctance $L = 10$ mH, $\theta = 150°$. In Fig. 15, at time t_1, the proposed control method is replaced with the basic branch current allocation and at time t_2, the proposed control is restored. These results verify the effectiveness of the proposed balancing control and Fig. 16 shows that there is no reactive power at the ac grid side of the converter.

B. Branch Current Stresses Verification

As explained in Section IV-C, branch current stresses can be calculated according to (64). Fig. 17 shows the comparisons

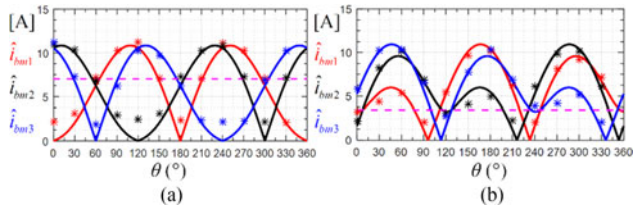

Fig. 17. Branch current stresses verification. (a) With $R = 5\ \Omega$ and $L = 0$. (b) With $R = 5\ \Omega$ and $L = 10$ mH.

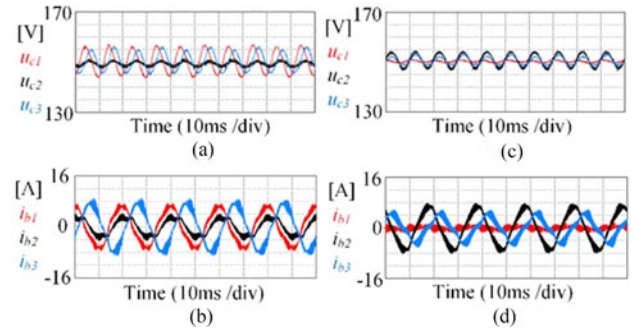

Fig. 18. Capacitor voltages and branch currents with $R = 5\ \Omega$ and $L = 0$. (a) Capacitor voltages when $\theta = 150°$. (b) Branch currents when $\theta = 150°$. (c) Capacitor voltages when $\theta = 180°$. (d) Branch currents when $\theta = 180°$.

between the calculated and experimental results. The output fundamental frequency is set as $f_2 = 50$ Hz. In Fig. 17(a) and (b), the loads are $R = 5\ \Omega$ $L = 0$ and $R = 5\Omega$ $L = 10$ mH, respectively. The solid lines are the calculated branch current stresses of Branchs 1, 2, and 3. The experiments are performed every 30° on horizontal axis. Experimental results are marked as "$*$." It can be seen that in Fig. 17(a) and (b), the branch current experimental results correspond to the calculated results well. Meanwhile, the dashed line in Fig. 17 is the maximum branch current stress under basic branch current allocation, which is calculated according to (63). Because of the increased reactive power at the output side, the branch current stresses increase more in Fig. 17(b) than in Fig. 17(a).

With load $R = 5\ \Omega$ and $L = 0$, take $\theta = 120$, 150, and 180 for example, the capacitor voltages and branch currents are shown in Fig. 13(c), (d) and Fig. 18(a)–(d). With load R = 5 Ω and L = 10 mH, take $\theta = 120$, 150, and 180 for example, the capacitor voltages and branch currents are shown in Figs. 19(a), (b), 15(c), (d), and 19(c),(d).

C. Near Equal-Frequency Verification

The results above validate the theoretical analysis and the effectiveness of the proposed control method under equal frequency operation ($f_1 = f_2 = 50$ Hz). Fig. 20 shows the results when there is a small difference between the input and output frequencies. The output fundamental frequency, here, is set as $f_2 = 49.5$ Hz. In Fig. 20(a) and (b), the load is $R = 5\ \Omega$ $L = 0$. Before time t_1, the proposed branch-balancing method is applied. Capacitor voltages fluctuate around 150 V with a fluctuation of ± 10 V. At time t_1, the basic branch current allocation is applied instead. The magnitudes of the capacitor voltages fluctuation increase immediately. The voltage fluctuations in-

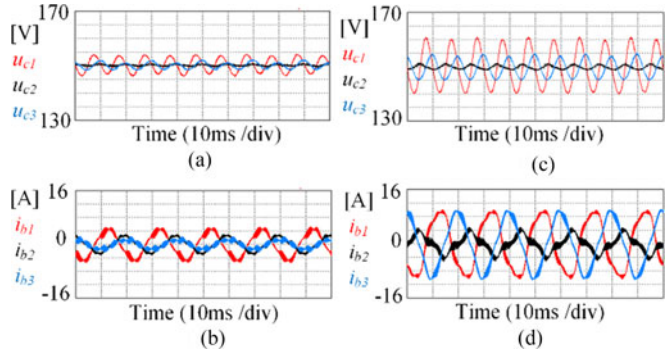

Fig. 19. Capacitor voltages and branch currents with $R = 5\ \Omega$ and $L = 10$ mH. (a) Capacitor voltages when $\theta = 120°$. (b) Branch currents when $\theta = 120°$. (c) Capacitor voltages when $\theta = 180°$. (d) Branch currents when $\theta = 180°$.

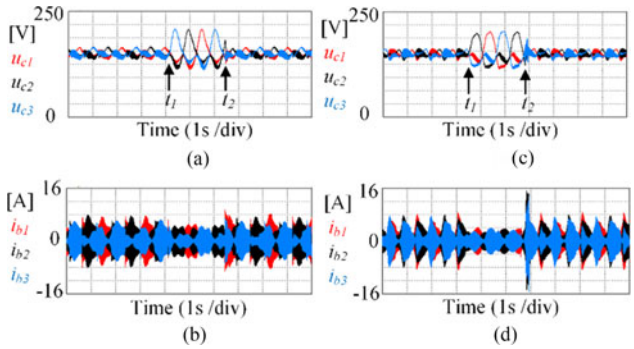

Fig. 20. Capacitor voltages and branch currents when the output frequency is 49.5 Hz. (a) Capacitor voltages with $R = 5\ \Omega$ and $L = 0$. (b) Branch currents with $R = 5\ \Omega$ and $L = 0$. (c) Capacitor voltages with $R = 5\ \Omega$ and $L = 10$ mH (d) Branch currents with $R = 5\ \Omega$ and $L = 10$ mH.

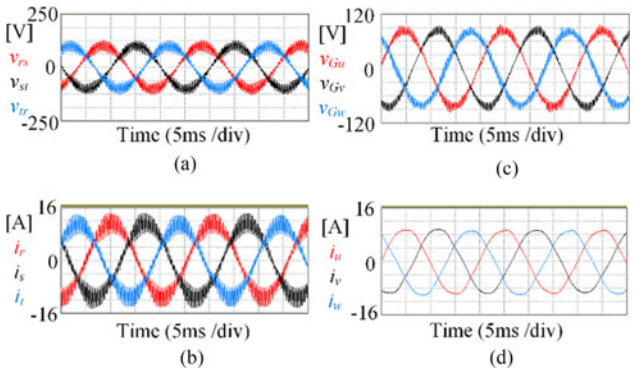

Fig. 21. Capacitor voltages balancing with $R = 5\ \Omega$ and $L = 0, f_2 = 49.5$ Hz. (a) Output line-to-line voltages. (b) Output currents. (c) AC grid phase-to-neutral voltages. (d) Input currents.

crease to +60 and –50 V. This consists with the branch power analysis. At time t_2, the proposed control is applied again and the capacitor voltages become effectively suppressed again. In Fig. 20(c) and (d), the similar experiment is performed when the load is $R = 5\ \Omega\ L = 10$ mH. In Fig. 20(c) and (d), before time t_1, the proposed branch-balancing method is applied. Capacitor voltages fluctuate around 150 V with a fluctuation of ± 10 V. At time t_1, the basic branch current allocation is applied instead. The magnitudes of the capacitor voltages fluctuation increase

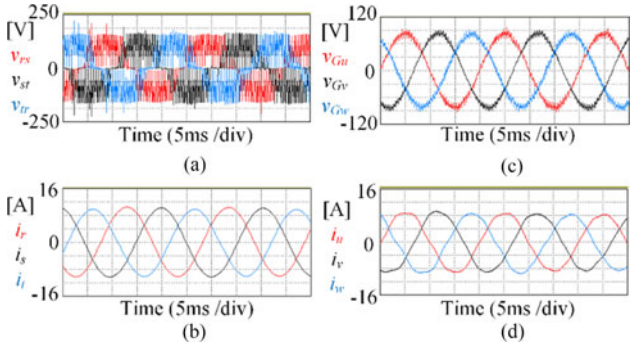

Fig. 22. Capacitor voltages balancing with $R = 5\ \Omega$ and $L = 10$ mH, $f_2 = 49.5$ Hz. (a) Output line-to-line voltages. (b) Output currents. (c) AC grid phase-to-neutral voltages. (d) Input currents.

immediately. At time t_2, the proposed control is applied again and the capacitor voltages become effectively suppressed again.

Figs. 21 and 22 show the three-phase voltages and currents. As the ac grid voltages are in phase with the input currents, there is no reactive power applied at the ac grid.

VI. Conclusion

In the M3C there are typically 3 DOF to solve the problem of close input and output frequency operation: reactive power at input side, common-mode voltage, and inner circulating currents. This paper discussed the possibility of using only the inner circulating currents to make M3C applicable for equal-frequency operation.

In order to confirm this consideration, a theoretical analysis was first presented in the phasor domain to develop an adjusted branch current allocation to stabilize the branch energy, which proved the consideration is available when the magnitudes of the input and output voltages are not similar. The branch power fluctuations were suppressed effectively with the application of the reallocated branch currents. Meanwhile when the input and output voltage share a similar magnitude, the consideration is only possible with a purely resistive load. Therefore, a branch energy balancing control method based on branch current reallocation in phasor domain was proposed. Experimental results validated the theoretical analysis and proved that the low frequency capacitor voltage fluctuations can be effectively suppressed with the proposed control method while keeping unity power factor at the ac grid side and without using common-mode voltage.

References

[1] R. W. Erickson and O. A. Al-Naseem, "A new family of matrix converters," in *Proc. 27th Annu. Conf. IEEE Ind. Electron. Soc.,* 2001, vol. 2, pp. 1515–1520.

[2] H. Akagi, "Classification, terminology, and application of the modular multilevel cascade converter (MMCC)," *IEEE Trans. Power Electron.*, vol. 26, no. 11. pp. 3119–3130, Nov. 2011.

[3] F. Kammerer, J. Kolb, and M. Braun, "Fully decoupled current control and energy balancing of the Modular Multilevel Matrix Converter," in *Proc. 2012 15th Int. Power Electron. Motion Control Conf.*, 2012, pp. LS2a.3-1–LS2a.3-8.

[4] W. Kawamura, M. Hagiwara, and H. Akagi, "A broad range of frequency control for the modular multilevel cascade converter based on triple-star bridge-cells (MMCC-TSBC)," in *Proc. 2013 IEEE Energy Convers. Congr. Expo.*, 2013, pp. 4014–4021.

[5] W. Kawamura, M. Hagiwara, and H. Akagi, "Control and experiment of a modular multilevel cascade converter based on triple-star bridge cells (MMCC-TSBC)," *IEEE Trans. Ind. Appl.*, vol. 50, no. 5. pp. 3536–3548, Sep./Oct. 2014.
[6] F. Kammerer, M. Gommeringer, J. Kolb, and M. Braun, "Energy balancing of the Modular Multilevel Matrix Converter based on a new transformed arm power analysis," in *Proc. 2014 16th Eur. Conf. Power Electron. Appl.*, 2014, pp. 1–10.
[7] M. Hagiwara, K. Nishimura, and H. Akagi, "A medium-voltage motor drive with a modular multilevel PWM inverter," *IEEE Trans. Power Electron.*, vol. 25, no. 7. pp. 1786–1799, Jul. 2010.
[8] K. Wang, Y. Li, Z. Zheng, and L. Xu, "Voltage balancing and fluctuation-suppression methods of floating capacitors in a new modular multilevel converter," *IEEE Trans. Ind. Electron.*, vol. 60, no. 5. pp. 1943–1954, May 2013.
[9] A. Antonopoulos, L. Angquist, S. Norrga, K. Ilves, L. Harnefors, and H. P. Nee, "Modular multilevel converter AC motor drives with constant torque from zero to nominal speed," *IEEE Trans. Ind. Appl.*, vol. 50, no. 3. pp. 1982–1993, May/Jun. 2014.
[10] J. Kolb, F. Kammerer, M. Gommeringer, and M. Braun, "Cascaded control system of the modular multilevel converter for feeding variable-speed drives," *IEEE Trans. Power Electron.*, vol. 30, no. 1. pp. 349–357, Jan. 2015.
[11] K. Ilves, L. Bessegato, and S. Norrga, "Comparison of cascaded multilevel converter topologies for AC/AC conversion," in *Proc. 2014 Int. Power Electron. Conf.*, 2014, pp. 1087–1094.
[12] B. Bednar, P. Drabek, and M. Pittermann, "The comparison of different variants of new traction drives with medium frequency transformer," in *Proc. 2016 Int. Symp. Power Electron., Elect. Drives, Autom. Motion*, 2016, pp. 1172–1177.
[13] Y. Okazaki *et al.*, "Which is more suitable for MMCC-based medium-voltage motor drives, a DSCC inverter or a TSBC converter?" in *Proc. 2015 9th Int. Conf. Power Electron. ECCE Asia*, 2015, pp. 1053–1060.
[14] F. Kammerer, D. Braeckle, M. Gommeringer, M. Schnarrenberger, and M. Braun, "Operating performance of the modular multilevel matrix converter in drive applications," in *Proc. Int. Exhib. Conf. Power Electron.*, 2015, pp. 1–8.
[15] S. D. G. Jayasinghe and D. M. Vilathgamuwa, "A modular matrix converter for transformer-less PMSG wind generation systems," in *Proc. 2011 IEEE 9th Int. Conf. Power Electron. Drive Syst.*, 2011, pp. 474–479.
[16] M. Diaz, R. Cardenas, B. M. Espinoza, A. Mora, and F. Rojas, "A novel LVRT control strategy for modular multilevel matrix converter based high-power wind energy conversion systems," in *Proc. 2015 10th Int. Conf. Ecol. Veh. Renewable Energies,* 2015, pp. 1–11.
[17] J. M. Apsley *et al.*, "Propulsion drive models for full electric marine propulsion systems," *IEEE Trans. Ind. Appl.*, vol. 45, no. 2, pp. 676–684, Mar.–Apr. 2009.
[18] D. Braeckle, F. Kammerer, M. Schnarrenberger, M. Hiller, and M. Braun, "A modular multilevel matrix converter for high speed drive applications," in *Proc. Int. Exhib. Conf. Power Electron., Intell. Motion, Renewable Energy Energy Manage*., 2016, pp. 1–8.
[19] Y. Miura, K. Inubushi, T. Yoshida, T. Fujikawa, and T. Ise, "Operation of modular matrix converter under close input and output frequency by using voltage space vector modulation," in *Proc. 41st Annu. Conf. IEEE Ind. Electron. Soc.*, 2015, pp. 5136–5141.
[20] W. Kawamura, Y. Chiba, M. Hagiwara, and H. Akagi, "Experimental verification of TSBC-based electrical drives when the motor frequency is passing through, or equal to, the supply frequency," in *Proc. 2015 IEEE Energy Convers. Congr. Expo.*, 2015, pp. 5490–5497.
[21] F. Kammerer, J. Kolb, and M. Braun, "A novel cascaded vector control scheme for the modular multilevel matrix converter," in *Proc. 37th Annu. Conf. IEEE Ind. Electron. Soc.*, 2011, pp. 1097–1102.
[22] W. Kawamura and H. Akagi, "Control of the modular multilevel cascade converter based on triple-star bridge-cells (MMCC-TSBC) for motor drives," in *Proc. 2012 IEEE Energy Convers. Congr. Expo.*, 2012, pp. 3506–3513.
[23] W. Kawamura, M. Hagiwara, and H. Akagi, "Control and experiment of a 380-V, 15-kW motor drive using modular multilevel cascade converter based on triple-star bridge cells (MMCC-TSBC)," in *Proc. 2014 Int. Power Electron. Conf.*, 2014, pp. 3742–3749.
[24] W. Kawamura, M. Hagiwara, and H. Akagi, "Experimental verification of a modular multilevel cascade converter based on triple-star bridge-cells (MMCC-TSBC) for motor drives," in *Proc. 1st Int. Future Energy Electron. Conf.,* 2013, pp. 454–459.
[25] R. Tsuruta, T. Hosaka, and H. Fujita, "A new power flow controller using six multilevel cascaded converters for distribution systems," in *Proc. 2014 Int. Power Electron. Conf.*, 2014, pp. 1350–1356.
[26] M. P. Kazmierkowski and L. Malesani, "Current control techniques for three-phase voltage-source PWM converters: A survey," *IEEE Trans. Ind. Electron.*, vol. 45, no. 5. pp. 691–703, Oct. 1998.
[27] M. Hagiwara and H. Akagi, "Control and experiment of pulsewidth-modulated modular multilevel converters," *IEEE Trans. Power Electron.*, vol. 24, no. 7, pp. 1737–1746, Jul. 2009.

Boran Fan (S'13) was born in Tianjin, China, in 1989. He received the B.S. degree in electrical engineering from the Department of Electrical Engineering, Tsinghua University, Beijing, China, in 2013. He is currently working toward the Ph.D. degree in the Department of Electrical Engineering, Tsinghua University.

His current research interests include topology and control of multilevel converters.

Kui Wang (M'11) was born in Hubei, China, in 1984. He received the B.S. and Ph.D. degrees in electrical engineering from the Department of Electrical Engineering, Tsinghua University, Beijing, China, in 2006 and 2011, respectively.

He is currently a Faculty Member in the Department of Electrical Engineering, Tsinghua University. His research interests include topology and control of multilevel converters, renewable energy generation, and wide band-gap semiconductor.

Pat Wheeler (SM'11) received the B.Eng. (Hons.) degree and the Ph.D. degree in electrical engineering for his work on matrix converters from the University of Bristol, Bristol, U.K., in 1990 and 1994, respectively.

In 1993, he joined the University of Nottingham as a Research Assistant in the Department of Electrical and Electronic Engineering. In 1996, he became a Lecturer in the Power Electronics, Machines and Control Group, University of Nottingham, Nottingham, U.K. Since January 2008, he has been working as a Full Professor in the same research group. He is currently the Head of the Department of Electrical and Electronic Engineering, University of Nottingham. He is an IEEE PELs 'Member at Large' and an IEEE PELs Distinguished Lecturer. He has published 400 academic publications in leading international conferences and journals.

Chunyang Gu (S'12–M'15) was born in Heilongjiang, China, in 1988. She received the B.Sc. degree in electrical engineering from the Harbin Institute of Technology, Harbin, China, in 2010 and the Ph.D. degree in electrical engineering from the Department of Electrical Engineering, Tsinghua University, Beijing, China, in 2015.

She is currently a Research Fellow in Power Electronics, Machines and Control Research Group, University of Nottingham, Nottingham, U.K. Her current research interests include solid-state circuit breakers, power converter topologies and control, multilevel power converters, solid-state transformers, and application of WBG semiconductor devices.

Yongdong Li (M'08) was born in Hebei, China, in 1962. He received the B.S. degree in electrical engineering from Harbin Institute of Technology, China, in 1982 and the M.S. and Ph.D. degrees in electrical engineering from the Department of Electrical Engineering, Institut National Polytechnique de Toulouse, Toulouse, France, in 1984 and 1987, respectively

Since 1996, he has been a Professor in the Department of Electrical Engineering, Tsinghua University, Beijing, China. His research interests include power electronics, machine control, and wind power generation.